annalen der **physik**

Nanoplasmonic structures for biophotonic applications: SERS overview

Anisha Gopalakrishnan[1,2], *Mario Malerba*[1,2], *Salvatore Tuccio*[1,2], *Simone Panaro*[1,2], *Ermanno Miele*[1,2], *Manohar Chirumamilla*[1,2], *Stefania Santoriello*[1], *Carla Dorigoni*[1], *Andrea Giugni*[1], *Remo Proietti Zaccaria*[1], *Carlo Liberale*[1], *Francesco De Angelis*[1], *Luca Razzari*[1], *Roman Krahne*[1], *Andrea Toma*[1], *Gobind Das*[1,*], and *Enzo Di Fabrizio*[1]

Various nanoplasmonic devices were fabricated using *top-down* method such as electron beam lithography, electroplating and focused ion beam techniques. These substrates were investigated after depositing the molecules from dye to protein, using chemisorptions techniques. Theoretical simulations were also performed on these model nanostructures in order to understand the electrical field distribution. Furthermore, the future prospects of these nanostructures were also mentioned in this report.

1 Introduction

Nanoplasmonics, a branch of nano-optics, is a topic that has seen an exponential growth over the past few decades. Its remarkable advantage is the nanometric scale onto which electric and electromagnetic fields can concentrate and propagate, reaching dimensions that go well beyond the diffraction limit [1–3]. Surface plasmons (SPs), in detail, are pure surface electron oscillations, and their localization is in principle limited only by the dimension of the nanostructure itself. In a way, metallic nanostructures act as concentrators of optical energy, harvesting and localizing it in specific *hotspots*, or active sites, where the electric field can be greatly enhanced [4, 5]. Furthermore, nanoaggregates of several nanoparticles, and engineered nanostructures placed in tight contact, exhibit an anomalous giant field in the interparticle gap, reaching values that enhance up to 10^2–10^3 times the incoming field [6].

One of the most interesting applications of this phenomenon is surface enhanced Raman spectroscopy (SERS) [7], a technique which employs specially nanostructured metallic substrates, and is able to study the fin-gerprint of molecular bonds despite the intrinsic weakness of the signal. Pioneered by Fleishmann [8] and Van Duyne [9], SERS has seen itself a parallel boost, along with the development of nanopatterning techniques and nanofabrication in general. Although some aspects have not yet been completely explained, the accepted mechanism explaining Raman signal enhancement takes into account both a chemical and an electromagnetic effect. The former mechanism, of chemical nature, is connected to molecular polarizability, and to the charge transfer between electronic states in the molecules; the latter, of electromagnetic nature, is mediated by surface plasmons, enhancing the number of scattered photons. Because of these two combined effects, the scattering cross-section can be improved by many orders of magnitude, proportional to local field $|E_{loc}|^4$; therefore, since in some hotspots $|E|/|E_0| = 10^3$ and the SERS enhancement factor is proportional itself to a fourth power, the total Raman scattering enhancement theoretically becomes $g^{SERS} \simeq 10^{12}$ [3].

This result is quite interesting; in fact it allows overcoming, to a certain extent, two of the major issues of traditional Raman spectroscopy: low scattering cross-section and low signal-to-noise ratio. The major drawback of traditional Raman spectroscopy is, in fact, the high laser power needed, or the high integration times, often leading to a damage, or modification, of the samples. Organic samples are especially sensitive to the source power, and SERS dramatically reduces stress/-

---

* Corresponding author and team leader   E-mail: gobind.das@iit.it, Phone: +39-010-71781-217, Fax: +39-010-720321
[1] Nanostructures Department, Istituto Italiano di Tecnologia, Via Morego 30, 16163 Genova, Italy
[2] Università degli Studi di Genova, 16145 Genova, Italy

WILEY ONLINE LIBRARY

damage on biological samples; furthermore, it reduces substantially the background signal, which often is so high that it hides some of the molecular signature peaks. Although its origin is not yet completely understood, main causes are believed to be inelastic scattering from surface roughness, molecule luminescence and laser burning of carbon contaminants [10]. SERS, however, reduces significantly this part of the spectrum, enhancing only the signal arriving from the hotspots (e.g. molecules adsorbed in the gaps between the metallic nanostructures). Thanks to these advantages and features, this technique becomes a candidate for few-molecules detection, opening new paths for efficient biosensors for early disease diagnosis [11–13].

2 Methods: simulation, fabrication and trends

Following the achievements in the fields of nanofabrication and characterization at the nano-scale, novel plasmonic devices with complex 3D geometries have become possible. As a consequence, in the last decades engineering of plasmonic structures has experienced a strong effort and an exponential growth. A solid and valuable classical physical background exists, but analytical methods are often unable to solve complicated geometries; in most of cases, these can be approached through numerical methods, thanks to today's powerful computational availability, distributing space into finite elements and solving Maxwell's equations.

There are two algorithms commonly used in commercial software: FDTD (Finite Difference Time Domain) and FEM (Finite Element Method). The first is based on solving both, electric and magnetic fields in temporal domain, using the full-vector differential form of Maxwell's equations. The entire computational domain needs to be gridded and Maxwell's time-dependent equations are discretized [14]. The second is a numerical technique which obtains approximate solutions to boundary-value problems of physics based on few main steps: discretization of the simulation domain into subdomains, selection of the interpolation functions for unknown functions in the subdomains and representation with unknown coefficients, formulation of the system equations and its solution [15]. In comparison, transient response and impulse field effects are more precisely solved by FDTD method, while objects with complex geometry and curved surfaces are better modeled with FEM, due to its adaptive mesh. Simulation and modeling however have to take into account limits and difficulties of fabrication: compromises must be accepted, and very often deviations from designed structures must be tolerated, especially regarding surface roughness and feature sharpness. In recent years, the fabrication methodology has improved remarkably, producing precise and complex structures and guaranteeing high reproducibility. Two different approaches are gen-
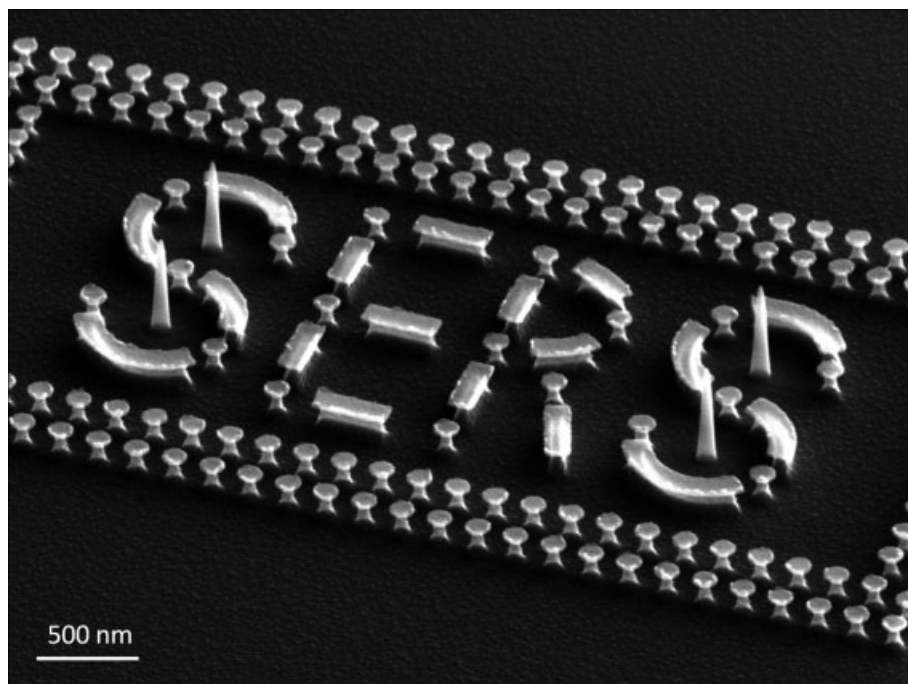

Figure 1 SEM image of Gold pillars, antenna and nanocones on Si wafer, fabricated by the combined techniques of electron beam lithography (EBL), reactive ion etching (RIE) and focused ion beam (FIB).

erally followed to produce SERS-active substrates: *top-down*, involving highly technological instrumentation for nanofabrication (Electron Beam lithography (EBL), Focused Ion Beam (FIB), metal evaporation/deposition), and *bottom-up*, involving mostly chemical approaches, such as self-assemblies of metallic nanoparticles, or electrochemical growth/etch of random structures. In general, a *top-down* approach guarantees an ordered, engineerable set of nanostructures, limiting randomness and ensuring reproducibility [16–21]. The drawback is, of course, a low throughput and a minimum resolution which is limited not by the underlying physics, but by the state of art of technological achievements; on the other side, the *bottom-up* approach can produce very large active areas, but is governed by the laws of chemistry and self-assembly, thus is heavily affected by boundary conditions, leading to randomness and high system entropy [22, 23].

The wide range of top-down techniques developed in the last decades has furthermore allowed the manipulation of 3D nanostructures [24], giving rise in the last 10 years to a special class of plasmonic devices used for enhanced Raman spectroscopy known as TERS, a subclass of SPM (scanning probe microscopy): despite a variety of different configurations to reach an optimized coupling of light to plasmon oscillations, the common denominator is a metallic tapered waveguide with some light-to-plasmon coupling feature (e.g. gratings), able to confine optical energy in a narrow hot spot not bigger than few tens of nanometers. The combination of these devices with traditional microscopes or with micromanipulation techniques has very recently given birth to the possibility of selecting the area of interest to be investigated with Raman spectroscopy, in principle even on biological specimen, with a resolution confined in the nanoscale. Recently, a new fabrication design (tapered waveguides for surface plasmon polariton Raman enhanced spectroscopy (SPPERS), where plasmon excitation is produced far away from the sensing apex) was developed by De Angelis et al. [25], to fully integrate the tapered waveguide onto an AFM cantilever without the use of gratings, primary source of noise in the signal. In a way, the sensor scans and finds the feature of interest, and analyzes, or chemically maps, a selected part of it.

An opposite approach is used when it comes to the detection of molecules in low concentration, because the capture of the analyte is limited by diffusion time: to make an example, a 10 nm sensor would in principle statistically need 1 year to capture 100 molecules from a 1fM solution [26]. To overcome this limit, the combination of SERS/TERS-active substrates with superhydrophobic surfaces has allowed concentrating the analyte in one single predicted hotspot, bringing closer the milestone of single/few molecules detection [27, 28]. In a way, in this second case, the molecules directly reach the sensor, thanks to the engineered substrates and the smart delivery.

3 Results and discussion

We report various kinds of enhanced Raman devices: the goal is to give some detailed examples of what can be done, following different approaches, showing the potential of every route. We explored anodic porous alumina, nanogold aggregates and Si porous nanoparticles, as examples of bottom-up fabrication, nanoantennas (also in the perspective of working in the THz domain), as an example of 2D top-down fabrication, and SPP tapered waveguide as an example of 3D top-down fabrication. SERS substrates were fabricated by means of electron beam lithography, combined with electro-plating techniques or physical depositions, whereas SPPERS devices were produced by combining focused ion beam and electron induced chemical vapor deposition. Various molecules were deposited on the substrates and then analyzed. Numerical modeling for all proposed devices was also carried out.

3.1 Large area SERS substrate: APA nanostructures

Anodic porous alumina (APA) with honey comb structure is a self ordered nanomaterial, fabricated by anodization process of aluminium. The important and admirable property of gold coated APA is that it can be fabricated in a large area, the location of the hot spot is well defined and it is very cheap to fabricate. Though the regular patterned structures are fabricated by electron beam lithography [29] cost wise it is not cheap to fabricate the device besides good reproducibility [30]. The interest of the design is that the sharp edges are the place of high electromagnetic field, in our case this acts as good template to detect the molecules and to enhance the Raman signal. The fascinating capacity of the substrate is its efficiency to quench the fluorescence background [31]. Hence the nano patterned hexagonal structure [32, 33] is of particular interest to see the enhanced Raman signals of the molecules. The technique to fabricate APA template was known in way back 1970's, but it's an innovative way to employ it as SERS substrate to detect variety of molecules from dyes to fluorescent proteins [31, 34]. It is well understood from the examination of such wide Ra-
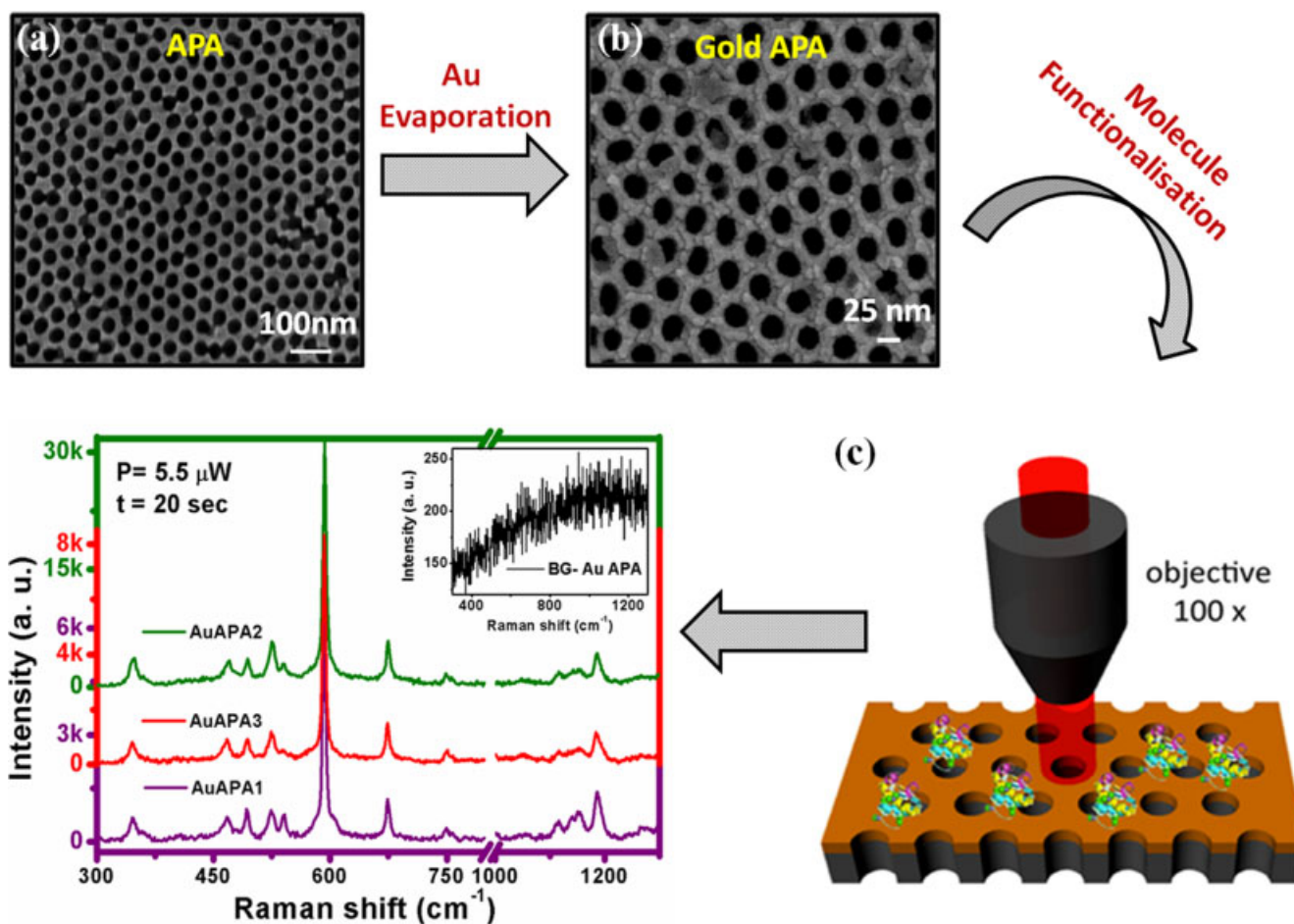
Figure 2 (online color at: www.ann-phys.org) (a) and (b) Represent SEM images of APA substrate before and after Au evaporation respectively. (c) A cartoon representation of APA sample under laser beam irradiation. The objective and laser spot size are not in scale for clarity reasons. During Raman measurements, the total area under illumination was 0.785 μm^2. (d) SERS spectra acquired on three different substrates are reported.

man spectral ranges, the metal substrate acts as a good SERS substrate which helps to understand the chemical vibration of the molecule. The substrates have hexagonal periodicity with different pore diameters and wall thickness based on the different acids in the anodization process. The novelty of this substrate fabrication is the reproducible SERS substrate down to 15 nm (wall thickness) and 40 nm (pore diameter).

The substrate of three different pore sizes and wall thicknesses of the same geometry is made possible by just changing three different acid electrolytes. SERS device is fabricated in two steps; (1) anodization to prepare the APA template with three different pore sizes by changing the acids viz., phosphoric, oxalic and sulfuric acid, and (2) to make it SERS active with thermally evaporated 25 nm gold layer over the APA template as it is shown in the Fig. 2(a,b). Finally, three different size templates are named as AuAPA1, AuAPA2, AuAPA3 and SERS measurements were done on it by attaching cresyl violet (CV), Rhodamine6G (R6G) molecules and GFPmut2 protein by means of chemisorption technique, through which a monolayer of the molecules under investigation is formed. CV molecules SERS spectra are used, to calculate the enhancement factor (E.F.) of the substrates which is based on the pore size and wall thickness of the templates. CV molecule's vibrational band intensity at 591 cm^{-1} (combination of in-plane N–H$_2$ and ring bending) is taken for the calculation. In Fig. 2(d), the SERS spectra of all three substrates are shown. AuAPA2 shows higher E.F. due to the high electric field which is based on the size and interparticle distance than the other two substrates in which the Computer Simulation Technol-
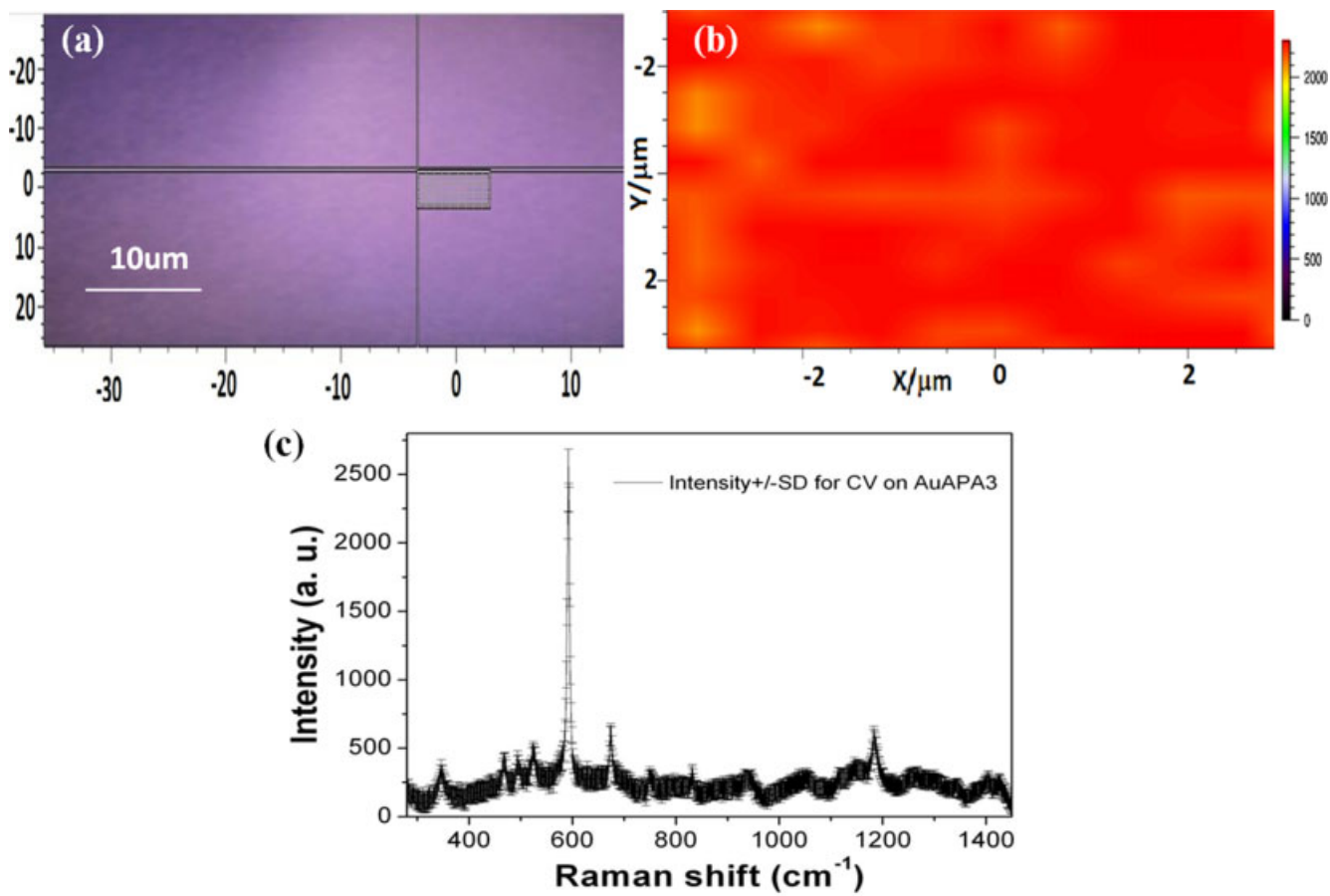
Figure 3 (online color at: www.ann-phys.org) (a) Optical image of the sample (AuAPA3) and the crossed area is the place where the mapping was performed. (b) The analysis is performed for the Raman band of CV centered at 591 cm^{-1} (λ-633 nm, $P = 27.5$ μW, $t = 1$ sec).The mapping analysis is done to show the spectral reproducibility of the enhancement factor (c) SERS spectrum of CV with the standard deviation for all the spectra.

ogy (CST) calculation is also in agreement. In order to have a statistical data and to show the SERS reproducibility from the substrates, mapping measurements are also performed on three substrates. The optical image of the mapped area, its image analysis with respect to the Raman band 591 cm^{-1} and the standard deviation of the SERS spectrum of AuAPA3 is shown in Fig. 3(a,b) and (c) respectively.

Numerical simulations have been performed in order to provide the analysis for the electromagnetic characterization of Au nanostructures supported by APA template by means of CST microwave Studio [35]. A 25 nm thick layer of gold over honey-comb pattern with different periodicity of 260, 100 and 55 nm, and sub-wavelength air holes [36] with a diameter of 160, 60 and 15 nm, respectively, was considered for the simulations. The illumination source is an electromagnetic continuous wave with

a 633 nm wavelength and linear polarization along the x-axis. The sketch of the simulated structure is represented in Fig. 4a. The electric field depends on the material discontinuity, since the absolute value of the field amplitude shows some zeros at gold-air interface, as one can see from the z-component of the electric field in Fig. 4b. In fact, the anti-phase hot spots along the x-axis, created by the x-polarization, determine the change in the electric field intensity (Figs. 4(c–e)). Normalized electric field distribution was represented with red color for the maximum and blue color for the minimum. In Figs. 4(f–h) are shown the relative electric field profiles over the gold surface for all the AuAPA substrates with respect to AuAPA3 substrate. In fact, the last one has a 90% of practical Raman signal, while AuAPA1 and AuAPA2 have respectively the 40% and the 30%. We can notice that the electric field intensity is proportional to the coupling strength be-
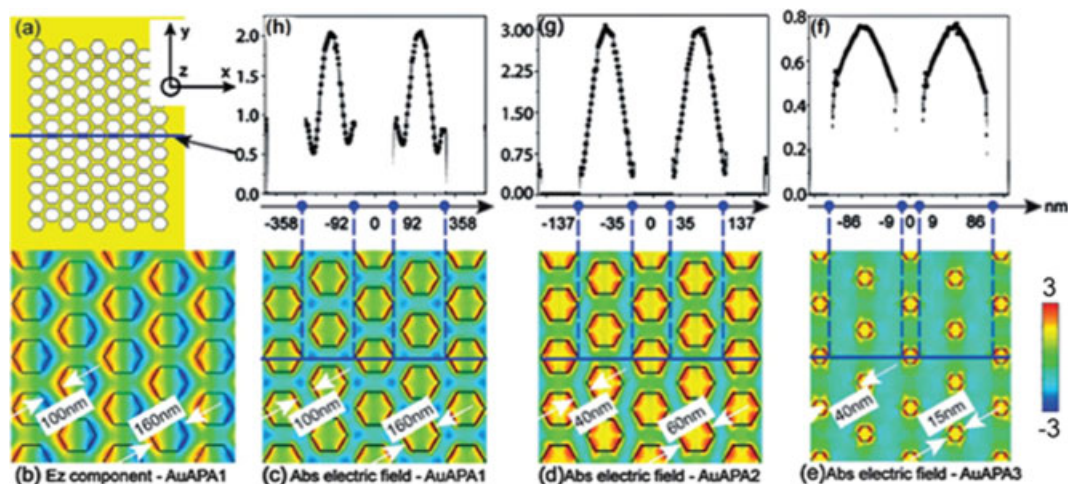
Figure 4 (online color at: www.ann-phys.org) CST simulations of honeycomb structures by varying pore size d and wall thickness $w (= D - d)$: (a) the prototype AuAPA structure; (b) amplitude of the z-component of the electric field in the $x-y$ plane of AuAPA1; the electric field distribution in the $x-y$ plane for (c) AuAPA1 with $d = 100$ nm and $w = 160$ nm, (d) AuAPA2 with $d = 60$ nm and $w = 40$ nm, (e) AuAPA3 with $d = 15$ nm and $w = 40$ nm; (f), (g) and (h) relative electric field profile over the gold surface along the highlighted line for all the SERS structures. The simulation was performed for the structure with the dielectric function of the gold slab $\varepsilon_{real} = -9.83$ and $\varepsilon_{imaginary} = 1.97$ [37].

tween the holes. Moreover the coupling decreases with the holes distance. This is particularly evident looking at the relative value of the electric field for all the samples. AuAPA2 substrate shows an electric field value remarkably higher than the AuAPA3 and AuAPA1 substrates. The simulations are in agreement with the experimental results.

The major aspects of using gold-coated APA as SERS substrates are its fluorescence quenching capacity, high SERS enhancement factor and the large area production of the substrate. The estimated SERS enhancement factor with respect to flat gold surface for λ-633 nm is $\sim 1.0 \times 10^4$. To demonstrate the substrate sensing response, various molecules were taken in consideration and their respective chemical vibrations were also studied in detail [31]. To emphasize the exclusive property of this device, it is an efficient and disposable biosensor.

3.2 Nanoantennas

Plasmonic devices find important application both in biophysics and in surface physics for their ability to localize and enhance the electromagnetic radiation. These properties can be exploited in several fields, ranging from bio-sensing [38] to Surface Enhanced Raman Scattering (SERS) [30] and terahertz spectroscopy [39]. The typical

goal of plasmonic devices for spectroscopy is the amplification of extremely low signals, improving the sensitivity of spectroscopic techniques even down to the single molecule level. In particular, this paragraph is dedicated to antenna devices, showing the main results obtained both from fabrication and optical point of view. As it was foreseen in the 60's by Richard Feynman [40], by scaling the system geometry, it is now possible to realize devices very similar to radio-wave antennas but working at much shorter wavelengths.

Plasmonic devices can support several order of resonance modes but, if the structures under consideration are smaller than the wavelength of incoming light, the dominant mode that can be excited is the dipolar mode. For elongated structures a Fabry-Perot like equation stands, taking into account the effective refractive index of the surface charge wave on the antenna [41]. In this approximation a quasi-linear dependence of the resonance wavelength on the length of such devices is found. Thus, antennas that are few hundred nanometers long resonate in the visible region. On the other hand, structures which are tens of micrometers long exhibit a resonance in the terahertz region.

As just mentioned, when the length of the antennas is in the range of few hundred nanometers, dipolar resonance arises in the visible/Near IR spectral region. Plasmonic enhancement effects at these frequencies find a

huge amount of applications for example in bio-sensing, spectroscopy and photovoltaics [42]. The strict correlation between geometry and optical response of plasmonic nanostructures implies that an asymmetrical geometry gives anisotropic transmission spectra. To confirm such symmetry considerations, making use of *Electron Beam Lithography*, matrices of antenna-like devices have been fabricated on CaF_2 substrates, chosen for their optical transparency in the spectral window of interest, obtaining structures with appreciable sub-wavelength reproducibility and clearly visible anisotropic shape (Fig. 5(a)).

Two single antennas can be coupled end-to-end, over a small gap, realizing antenna dimer configuration, as shown in Fig. 5(b). The transmission spectrum for polarization parallel to the long axis of the dimer can be checked while decreasing the size of the gap showing a gradual red-shift of the dipolar resonance wavelength. To interpret such a shift of the resonance wavelength one can consider the system as a pair of coupled harmonic oscillators. In fact, writing the characteristic equations of the two coupled oscillators associated to the charge distributions of each single arm of the dimer, a third spring connecting the two oscillators has to be included to take into account the near-field interaction between the antennas. Such term reduces the natural frequency of the uncoupled system or, in other words, coulombian forces

between the two arms of the dimer tend to slow down the motion of the surface charge wave. Because of the spatial dependence of these forces, such effect grows gradually while the dimer gap is decreasing. Resonance red-shift of antenna dimers with respect of single antennas is just one aspect of the near-field coupling. As a direct consequence of such effect, a huge field enhancement occurs within the gap at resonance, showing a very intense and localized *hot spot* [43].

Optical transmission measurements in far-field have been performed on such structures in the range between 400 nm and 900 nm. Plots in Fig. 5(c) show the transmission spectra of the above mentioned matrix of nanoantennas, for incident light with polarization respectively parallel and perpendicular to the long axis of the structures. By changing the polarization it is possible to appreciate the strong optical anisotropic behavior of such systems. Parallel polarization spectrum shows an extinction peak around 770 nm, while perpendicular polarization spectrum shows an analogue peak around 630 nm both induced by the excitation of localized plasmonic resonances, which is the typical behavior for sub-wavelength metallic structures [44]. The optical behavior of antenna-patterned surfaces makes them ideal plasmonic substrates for SERS (Fig. 5(d)). In fact, the resonances supported by these structures can match the wavelength of
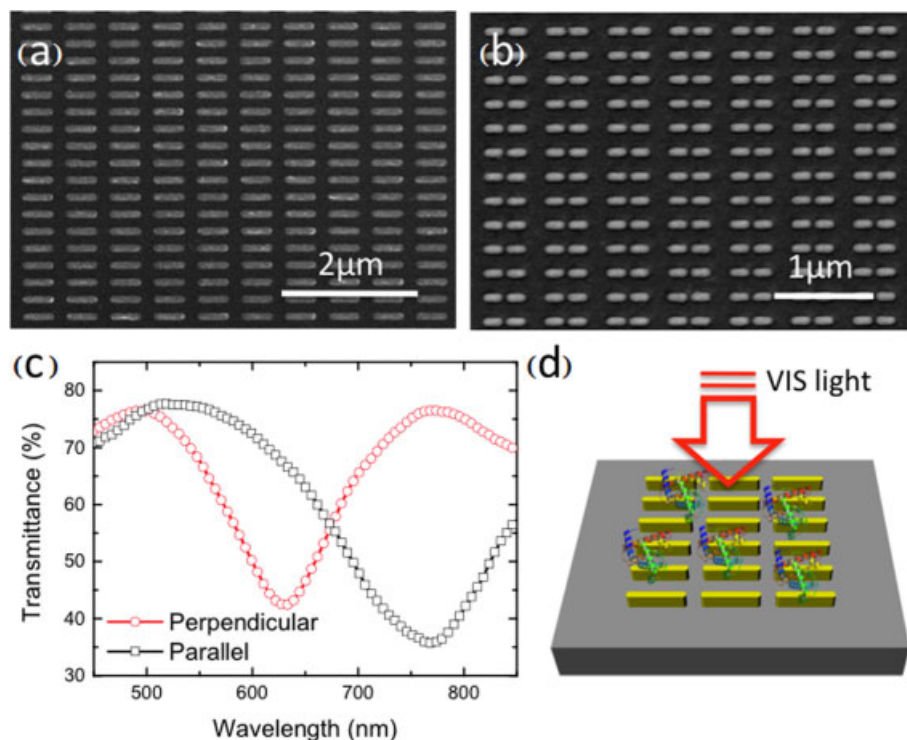

Figure 5 (online color at: www.ann-phys.org) (a) SEM image of a matrix of gold nanoantennas 410 nm long, 60 nm wide and high, (b) SEM image of a pattern of gold antenna dimers (arms 200 nm long with 40 nm gap), (c) far-field transmission spectra of gold antenna dimers for polarization parallel and perpendicular to the long axis of the structures, (d) schematic image showing molecules deposited on the top of an antenna pattern.

the lasers involved in such measurements, granting a significant enhancement of the Raman signal.

The application of these devices made advantage in the Raman spectroscopy and the sensing capability of nanoantenna device is checked by dipping the substrate in CV (3.46 μM in water for 15 min) molecule. Before dipping the CV solution the substrate is checked for purity by doing background measurements at several places of the substrates on the nanoantenna structures and also on the flat gold surfaces. The substrate is perfectly clean to proceed with further Raman spectra on it. In the background spectra except Ca-F vibration, no other vibrations are observed. The substrate is made to chemisorb CV molecule on it, so that uniform monolayer of the molecules can be obtained. Then the substrate is rinsed to remove the extra molecules which are not directly attached to the metal surface. SERS spectra of CV molecule on nanoantennas and on gold marker are shown in the Fig. 6. The sample was illuminated by laser line 633 nm for 50 sec. To check the substrate purity background measurements were done initially before depositing any CV molecule on it and it is shown in the Fig. 6 (black line). The SERS spectrum of the CV molecules has the prominent vibration of the band 591, 675 and 1189 cm^{-1} [45, 46]. It is clearly observed that the background is fluorescence quenched and there is a good enhancement in the Raman signals of CV molecules. The enhancement factor in this case is evaluated around 10^3 with respect to
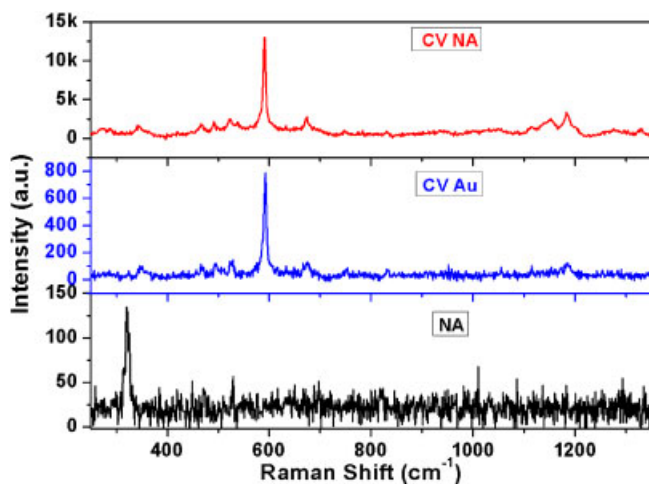

Figure 6 (online color at: www.ann-phys.org) SERS spectra of cresyl violet molecules deposited on nanoantenna (NA) sample (red line) and flat gold (blue line). Background measurement performed on bare NA structures is also shown (black line).

the flat gold surface, confirming nanoantenna-patterned devices are good substrate for sensing applications.

3.3 Nanogold aggregate

In this paragraph we acknowledge the fabrication of a device entirely dedicated to the detection of biomolecule (proteins) and to understand their thermodynamical behavior of all possible vibrations of the biomolecules. The substrate acts as a fluorescence quencher which is an added advantage of the plasmonic effect, an inherent property of the metallic nanostructures. The fluorescence background is quenched down so that the hidden weak vibrations are also observed along with the prominent vibrations of a molecule. The weak vibrations are studied to have a thorough relation with the temperature dependence intensity of the protein. To understand the variation of all possible vibrations of biomolecules, 2D- Correlation spectroscopy (2DCoS) were performed from the recorded spectrum [47, 48]. The 2D- correlation analysis is employed to understand the conformational changes within sample when it is subjected to an external perturbation while all other parameters of the system remain constant. Here we have made use of 2D synchronous method to analyze the peaks. In this case, the 2DCoS is used for spectral analysis, which makes it easy to correlate the spectral changes with respect to temperature. The important advantage of 2DCoS is its capacity to correlate the spectral bands with respect to the external excitation and also its deconvoluting capability. 2DCoS is a promising direct method to understand thermodynamical dependency of all possible strong and weak vibrations of the molecule. As probing molecules, we have chosen bovin serum albumin (BSA), lysozyme, ribonuclease-B, and myoglobin protein molecules for Raman analysis [30]. The wide range of molecules has been selected to understand their conformational behavior with respect to temperature (−65° to 90°C). One of the interesting things to be taken into account is the selection of off-resonance laser line (830 nm), which is specifically chosen to subsidies error caused in calculating secondary structures of protein in Raman analysis.

The substrate is fabricated by combining both EBL and electro-plating techniques. Disc like structures of empty discs with 80 nm diameter and 30 to 40 nm gap distance between two discs was fabricated by EBL. For gold growth in the empty disc (because of resist confinement), the substrate is dipped in the electrolytic system containing gold-potassium cynide and with the help of electroplating the device is fabricated [30]. SEM images
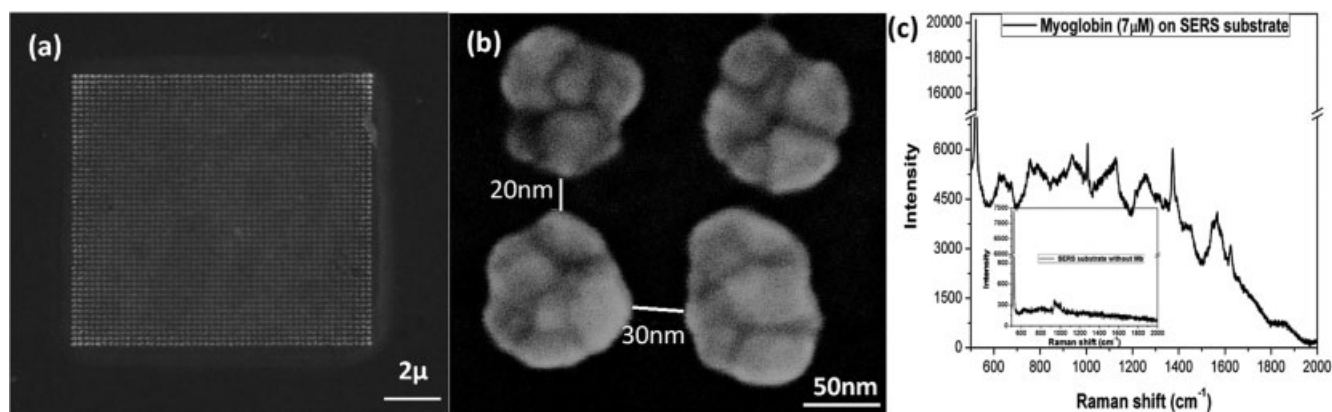
Figure 7 SEM micrographs of (a) array of fabricated nanoaggregates by EBL technique and (b) zoomed image of Au nanoaggregates selectively grown inside the nanohole pattern (c) SERS spectrum of myoglobin (Mb) protein is shown and the inset shows the background.

of the fabricated nanogold aggregate are shown in Fig. 7. The SERS substrate is then prepared by drop coating deposition Raman method [49].

The concentration of the biomolecules considered here is 7 μM. The SERS enhancement factor calculation is made for myoglobin (7 μM) spectrum. The myoglobin protein SERS spectrum is shown in Fig. 7(c) and in the inset the Raman signal without any molecules is shown. In order to fully understand the electromagnetic properties of the realized SERS device, an array of Au-nanoaggregates was simulated to provide information on the distribution of the absolute value of the electric field inside the structure [30]. As it is identified in the structures, hot spots are present all over it which can be justified by the morphological irregularity of the device. The maximum electric field enhancement observed due to the combination of sharp edges and gap variability among the nanoaggregates (2–10 nm), is about 600 (with respect to the light source) with linearly x-polarized source at 830 nm (calculated).

The Raman spectra of BSA with respect to temperature in the range of 600–2000 cm^{-1} are shown in the Fig. 8. The intensity ratio of bands of 855 and 830 cm^{-1} vibration band is shown in Fig. 8(b). These vibration bands are dedicated to the Fermi resonance of tryptophan (Tyr) residues, which is sensitive to environment of hydrogen bonding present at the OH group. If the phenolic oxygen is acceptor atom in a strong H-bond, for the Tyr residues in proteins, the intensity ratio (I_{855}/I_{830}) stands around 2.5 whereas if the phenolic oxygen is a proton donor in a strong H bond, the value lies around 0.7. From intensity ratio curve, the protein always shows that the phenolic OH of Tyr residues serve both as acceptor and donor of H-bond [50]. However, going towards higher temperature, the phenolic-OH shows stronger donor at low temperature.

The intensity of phenyalanine (Phe) band centered at 1005 and 1033 cm^{-1} is reported in Fig. 8(c). In the Fig. 8(c,d) there is a decrease in intensity of *Phe* band by increase in temperature, which indicates the gradual change of Phe's surrounding with respect to temperature. To understand the bond vibrations of the molecule by changing the temperature, a difference Raman spectra of BSA molecule with respect to Raman Spectra of BSA molecule at room temperature is shown in Fig. 8(d).

The 2D correlation representation of BSA in the range of 600–1060 cm^{-1} and 1600–2000 cm^{-1} is shown in Fig. 9, in which the autopeaks at 625 and 645 cm^{-1}, 830 & 855, 940 cm^{-1} (Tyr doublet), 1005 & 1033 cm^{-1} and 1650–1700 cm^{-1}, are clearly observed. The appearance of autopeak indicates the significant variation in intensity of different bands with respect to temperature. It is located at the diagonal position, representing the extent of dynamic variations of spectral intensity at different temperatures. The peaks correspond to the conformational changes of the molecule and in both the Fig. 8(c) and 9(a), the intensity of the vibrational bands of the molecules at 1005 & 1033 cm^{-1} undergoes a steady decrease with temperature variation and this may arise because of the accumulation of water to surface residues of protein. The same trend of decrease in intensity of the bands 830 and 855 cm^{-1} in the 2DCoS is also observed which is attributed to Tyr residues [51].

We can conclude that the Au-nanograin provides a good SERS substrate for biomolecules (proteins) with the sensitivity down to attomole [30]. The 2DCoS also provided rarely visible bands and a complete understanding of all possible variation in vibrations related to the biomolecules with respect to temperatures, which is otherwise difficult in normal experiments.

3.4 Adiabatic compression

An interesting and relatively novel device, in principle capable of a breakthrough as a spectroscopic technique, is surface plasmon polariton (SPP) enhanced Raman spectroscopy (SPPERS). It is different from traditional TERS because we refer to compression behavior. In this case, the signal is produced far from the zone where the il-

lumination is focused. Analytically calculated and numerically simulated results by Stockman and coworkers [52], a metallic cone supports SPP propagation. Efficient coupling of light to plasmons is not a straightforward task, and usually the necessary difference in momentum is provided through gratings or acute corners. When this is accomplished, propagation along the surface of the conical waveguide exhibits peculiar characteristics, exploitable for enhanced Raman spectroscopy, leading to a super-focusing effect on the nanoscale. On one side, when the apex of the structure is approached, the wavenumber k increases in an inversely proportional manner with respect to the distance r from the apex:

$$k \propto \frac{1}{r}.$$

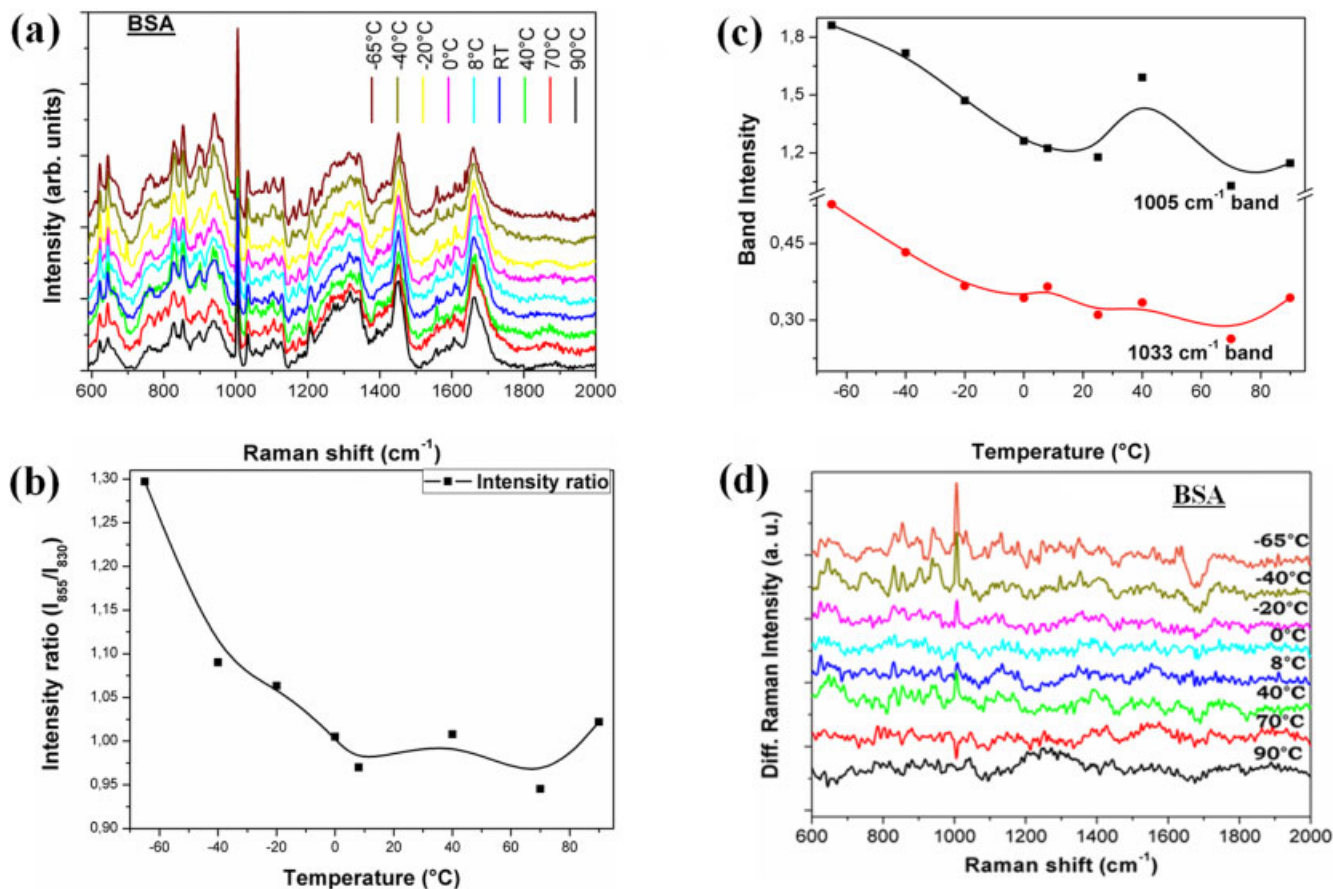This means that the wavelength is compressed, eventually to zero on the very tip of an ideal cone. As a direct

Figure 8 (online color at: www.ann-phys.org) (a) SERS spectra of BSA by varying the temperature in the range between −65 and 90°C; (b) intensity ratio (I_{855}/I_{830}) vs. temperature; (c) conformational change of Phenylalanine bands centered at 1005 and 1033 cm^{-1} by varying the temperature; and (d) difference Raman spectra of Bovine serum albumin (BSA) protein with respect to the BSA spectrum at RT.
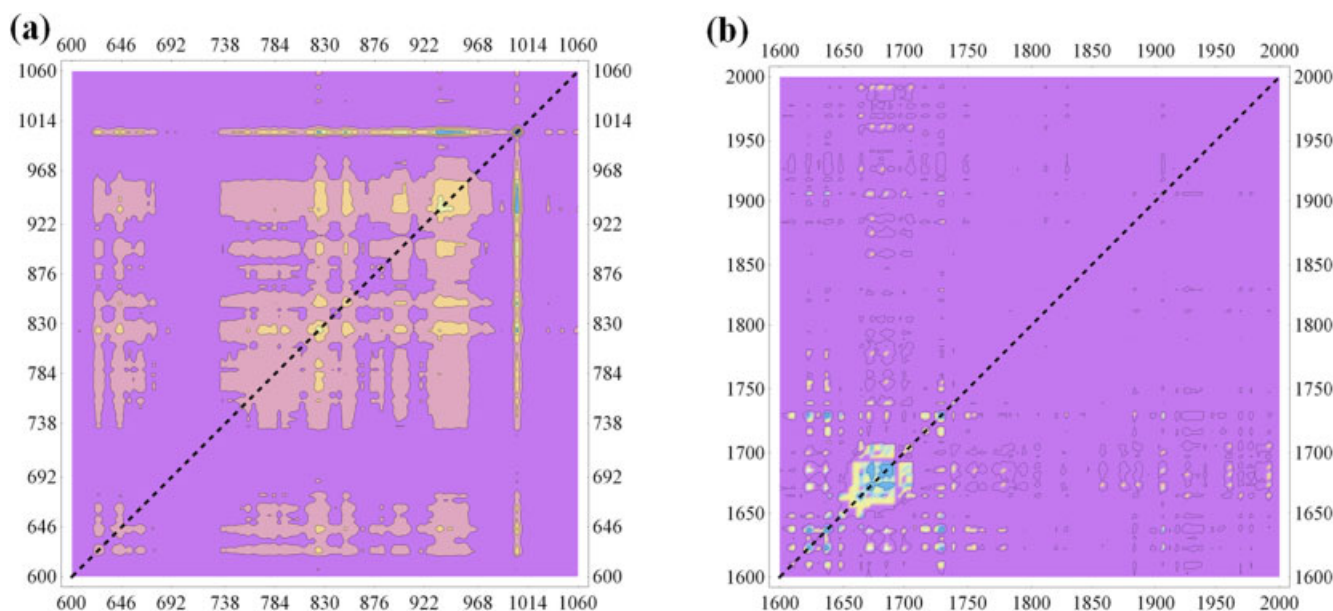
Figure 9 (online color at: www.ann-phys.org) 2D-correlation spectra in the range between 600–1060 cm^{-1} and 1600–2000 cm^{-1} of BSA molecule is shown in (a) and (b) respectively.

consequence, the group velocity slows down when approaching the apex.

On the other side, the electric field grows with a power law (see also [53]):

$$E_r \propto r^{-\frac{3}{2}}.$$

It is well known that the polarization of the incoming field is important to produce propagating modes. In particular TM$_0$ (or TM$_0$-like) distributions produce field enhancement on the apex. The role of polarization modes has been investigated through numerical simulations recently [54, 55]. The fingerprint of adiabatic compression is the phase and anti-phase symmetry of the three spatial
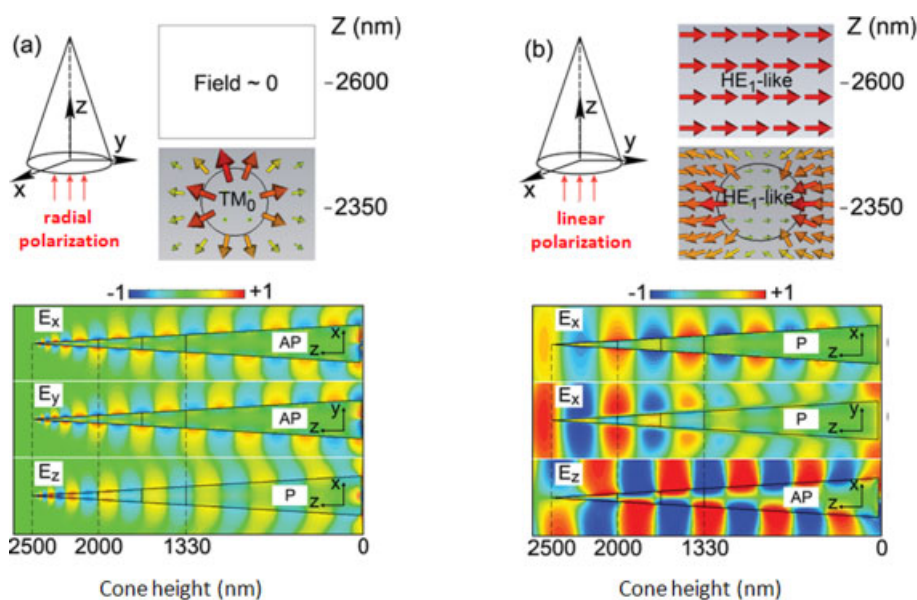

Figure 10 (online color at: www.ann-phys.org) Results are reported for radial and linear polarization (see [55]) impinging on a tapered waveguide. Cone height is $h = 2.5$ µm and base diameter is $b = 300$ nm; exciting laser source wavelength is $\lambda = 514$ nm. Upper part: sketch of simulated device and field direction/intensity (colour scheme in arbitrary units) 150 nm below the apex and 100 nm above the apex. Lower part: (a) phase and anti-phase electric field distribution for an axially-aligned and radially polarized beam, leading to adiabatic compression; (b) effects of an x-polarized plane wave source – no adiabatic compression is obtained. Both color scale bars indicate log($|E/E_0|^2$).

components, E_x, E_y and E_z, on the sides of the cone (see Fig. 10).

Absolute numerical values of the electric field on the cone, for both radially and linearly polarized source, are given in [56]. It is calculated that under radial polarization, a maximum field enhancement on the apex of an ideal cone could reach up to 400 times the incoming optical energy.

FDTD simulations have likewise been carried out on geometries resembling realistic devices, such as metallic conical tips built on AFM cantilevers (fabrication and experimental proof of concepts have been shown in [25] and [57]).

Both the cantilever and the substrate were considered in simulations. Figure 11 shows the electric field intensity and the enhancement for a realistic (curvature radius of the apex $r = 5$ nm) silver nanocone, excited with radial polarization ($l = 630$ nm). A Fresnel micro zone plate was also included and combined with this device, in order to have a self alignment.
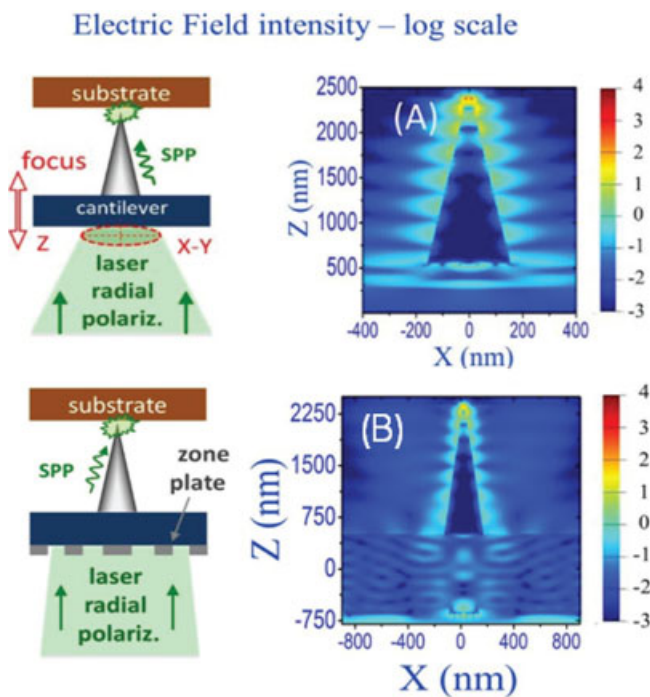

Figure 11 (online color at: www.ann-phys.org) Calculated electric field intensity for a real silver nanocone in proximity of a dielectric slab ($n = 1.5$, gap 0.5 nm) under radially polarized beam illumination; enhancement is shown to decrease from 110 to 71 by adding the zone plate, however focus or alignment mismatches weigh less.

Also linearly polarized laser beams can generate modes that allow adiabatic compression; plane waves are in fact much easier to produce, focus and use, but the lack of a radial symmetry does not itself produce a constructive configuration, and no adiabatic compression is obtained. A partial symmetry can be restored by introducing a phase shift, either by tilting the beam (Fig. 12(a), see also [58]), or fabricating a step, or a parallelepiped cavity, in the dielectric medium below the cone [see Fig. 12(b)]. The phase shift is optimized for a step of 315 nm, and produces a constructive phase / anti-phase configuration. At last, calculations were done for a cone built on a L3 cavity (three missing holes) in a photonic crystal, increasing enhancement to the detriment however of fabrication simplicity [see Fig. 12(c)]. Figure 12 shows a comparison of all devices.

4 Future perspectives on plasmonics

4.1 Advanced THz spectroscopy

A quite new and promising field in the nano-plasmonics scenario consists in the terahertz frequency regime because of its very interesting applications e.g. in spectroscopy [59], chemical identification [60] and non-destructive imaging. In fact, most dielectric materials, opaque for visible light, are practically transparent to THz radiation, moreover its low energy per photon prevents biological tissues from photoionization, allowing anyway the excitation of vibrational/rotational modes in several molecules.

Half-wavelength THz dipole nanoantennas can efficiently resonate at terahertz frequencies showing local field enhancement factors and extinction efficiencies of the order of hundreds.

By using high-resolution electron beam lithography technique an array of aligned planar gold nanoantennas was fabricated on a Si substrate (Fig. 13). In fact, Si presents high transparency and a constant value of refractive index in the THz region. The nanoantenna length has been chosen to be 40 μm, in order to have resonant behavior in a bandwidth around 1.5 THz, the width and height being respectively 200 nm (presenting a very high aspect ratio of 200) and 60 nm [39].

Inter-rod spacing, as shown in the large area SEM image, is randomized around a mean value of 20 μm, in order to average out the coupling among the antennas in the matrix, minimizing diffraction effects in the extinction measurements.
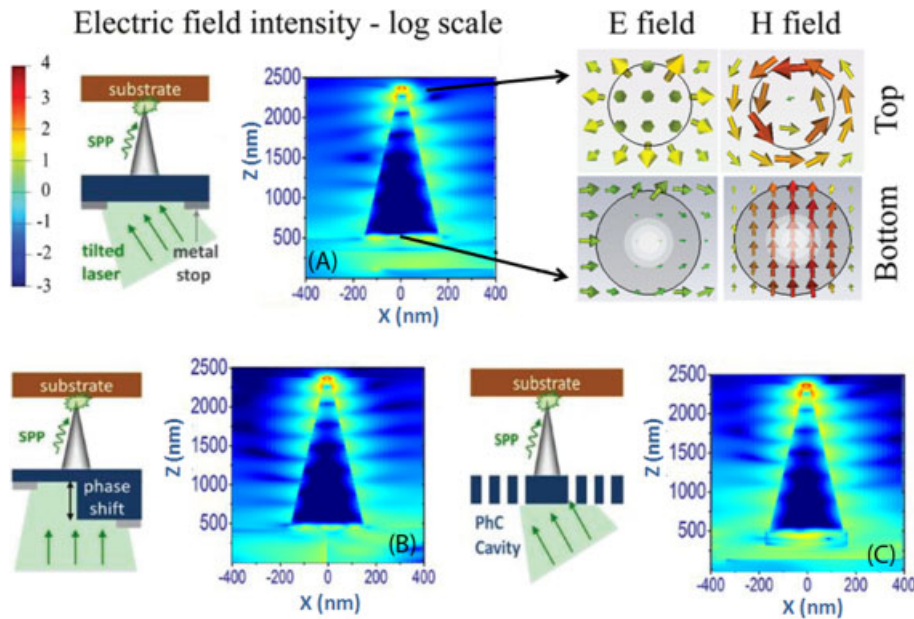
Figure 12 (online color at: www.ann-phys.org) Three possible solutions to produce TM_0-like polarization at the base of the nanocone, impinging with linearly polarized plane waves. Fabrication complexity increases along with enhancement factor. Colour scales are normalized to a single legend, and represent electric field intensity (log scale). (a) Tilting the beam creates a temporal phase shift, leading to adiabatic compression; on the right side, a plot of electromagnetic field direction on cone base and apex; (b) milled step into a Si_3N_4 cantilever, produces a $180°$ phase shift on one of the cone's corners, and adiabatic compression; (c) photonic crystal and L3 cavity, rearranging electromagnetic field distribution, and leading to efficient TM_0-like field distribution on the cone basis.

Far field extinction spectroscopy was used to characterize the fabricated sample [61], by using a standard zinc telluride source [62] producing quasi single-cycle terahertz pulses centered at 1 THz. The nanoantennas array was illuminated by a collimated terahertz beam with a beam diameter of 7 mm. THz pulses transmitted through the array (normal incidence) have been measured for the two cases of polarization set parallel and perpendicular to the long axis of the nanoantennas. Since the nanoantenna covering factor (ratio of the area covered by the nanoantennas divided by the overall illuminated area) is less than 0.4%, the array transmission in the case of polarization set along the short axis of the nanoantennas is found to be substantially identical to the one of a reference Si substrate with no nanoantennas. Due to this, it is possible to extract the resonance properties of the arrays by simply dividing the power spectrum of the transmitted pulse for long axis excitation by the one taken in the case of short axis excitation. The quantity thus obtained
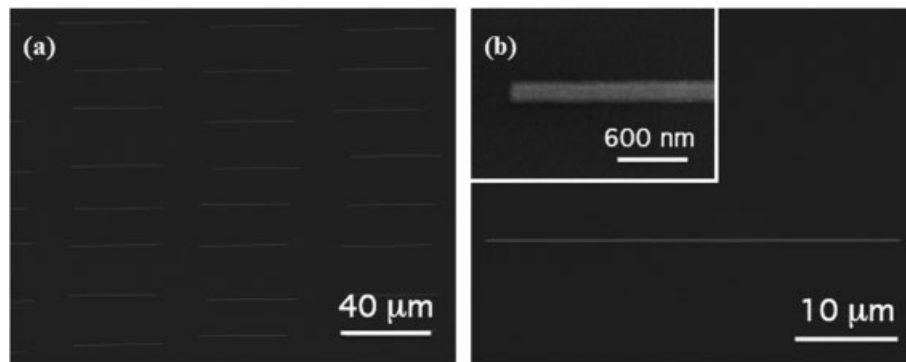

Figure 13 (a) SEM image of 40 µm long nanoantennas distributed with randomized periodicity, (b) SEM high-resolution image of a single nanoantenna (Inset: magnification of the nanoantenna apex). With permission of Optical Society of America.
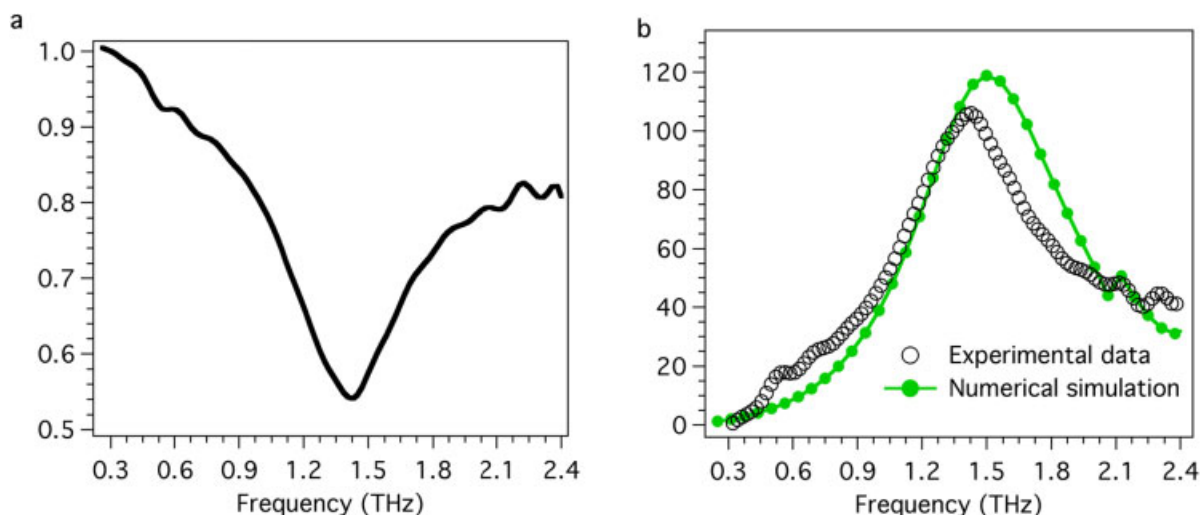
Figure 14 (online color at: www.ann-phys.org) (a) Relative transmission of the sample as a function of frequency, defined as the ratio of the transmitted spectrum for light polarized parallel to the long axis of the nanoantennas over the transmitted spectrum for perpendicular light polarization. With permission of Optical Society of America. (b) Comparison between experimental and numerically calculated extinction efficiencies of the sample, as a function of frequency. With permission of Optical Society of America.

is named "relative transmittance" (T_{rel}) and is reported in Fig. 14(a).

The relative transmission (shown in Fig. 14(a)) can be related with an important far field antenna parameter, namely the extinction efficiency Q_{ext} which qualitatively estimates the increase of the effective cross section of the antenna.

$$Q_{ext} = \frac{\sigma_{ext}}{\sigma_{geo}} = \frac{A(1 - T_{rel})}{NLD}. \tag{1}$$

In Eq. 1 A is the illuminated area, L and D the planar dimensions of the single device and N their number within the light spot.

In Fig. 14(b) experimental "Q_{ext}" (black trace) shows a clear peak at 1.4 THz, in correspondence to the extinction peak of the related transmittance spectrum, with a maximum efficiency of 100.

All simulation parameters are the same as the ones used in [39]. Numerical calculations were performed using a finite element method software [63]. The derived extinction efficiency is represented in Fig. 14(b) (green trace). We note that results are in good agreement with experimental values.

Simulations also provide near field properties of the nanoantenna. Figure 15(a) shows the absolute value of the electric field around the nanoantenna on a cut plane normal to the direction of the illuminating wave and positioned at the antenna half height. The field is highly localized at the nanoantenna ends. The full width at half maximum of the field distribution 1 nm away from the

nanoantenna end is 180 nm (inset in Fig. 15(b)), so that the incoming radiation is concentrated on a lateral size smaller than $\lambda/1000$.

Field enhancement factor as a function of frequency per definition F is reported in Fig. 15(b). A wide resonant behavior can be observed, with a maximum enhancement value of about 280 at around 1.3 THz.

The high field enhancement could be successfully employed for improving the sensitivity of THz spectroscopy. In fact, the effective absorption cross section of a molecule scales with $|F|^2$ and would thus be enhanced by several orders of magnitude in close proximity of the nanoantenna ends.

4.2 Nano-porous silicon

Nanostructured materials are important in various research field, owing to their unique features and unexplored potential. In this context, porous silicon (PSi) is paradigmatic: a simple and cheap fabrication process which allows the synthesis of porous particles whose characteristics are attractive even in plasmonics. Large surface area/volume is the key feature in nanostructured material. Hence, this characteristic is useful in a wide range of applications, from catalysis to diffusion process and SERS application [64–66].

PSi synthesis is an electrochemical hydrofluoric acid (HF) -based etching of Si. Several mechanisms have been
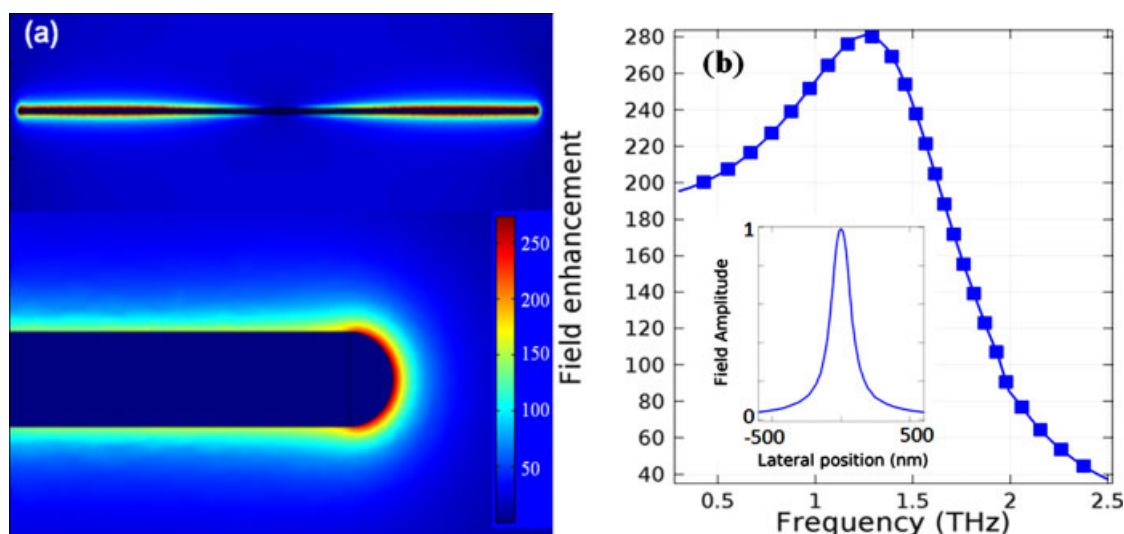
Figure 15 (online color at: www.ann-phys.org) (a) Contour plot of the absolute value of the electric field around the nanoantenna under resonant condition. (b) Field enhancement factor 'F' at the nanoantenna end as a function of frequency. Inset: normalized electric field profile close to the nanoantenna end.

proposed to explain this electrochemical reaction [67,68]: and one of the well known mechanism is in which fluorine atoms provide the charge displacement by attacking Si-Si bond and replaces the H atom in Si-H on the surface of Si layer. In this process holes play an important role by providing a site to attack fluorine. During this process hydrogen (H_2) is generated and the Si-Si lattice is randomly disrupted. Controlling the current density, the HF concentration and the transport properties (resistivity and doping) of the Si substrate, it is possible to tune the porosity (the fraction of voids in Si structure), the pore size and pore distribution, which in turn, are responsible of the surface area/volume ratio. Thus the anodization reaction results in porous silicon layer whose thickness, ranging from few nanometers up to several microns, can be controlled according to the anodization time. Nanometer pore structures in liquids undergo to very high surface tension forces, as predicted by Young-Laplace equation. For this reason it is fundamental to control wettability parameters (surface tension) to obtain continuous layers and homogeneous surfaces.

Among others, the characteristics feature of porous Si viz., biocompatibility and surface roughness are very attractive in the case of SERS applications. Roughness as well as porosity can be controlled on porous Si surface in order to have an active SERS surface. Though the Raman signal enhancement is based on the propagation of surface plasmons (the inherent property of the metal) and the chemical charge transfer mechanism, here, in the case of nanoporous Si, metal deposition e.g., gold/silver to be done to make it as a SERS substrate. Other than metals and metal deposited substrates, till date semiconductor quantum dot (e.g., CdTe [69]) is shown as a SERS active substrate in which the charge transfer mechanism is the basic cause of increment in Raman signal since there is no metal structure for the plasmonic effect.

Metallic surfaces, such as silver cluster, have superior plasmonic properties compared to porous Si but their employment in biological context is very limited by poor biocompatibility. On the other hand, PSi shows complete biocompatibility [70, 71] and large surface area available for chemical modification. Furthermore, PSi surface reactivity can be successfully exploited to perform electroless metal deposition. These combined features make PSi a suitable candidate for the fabrication of SERS sensors.

The controlled disintegration of PSi layers allows fabricating Nanoporous Silicon Nanoparticles (NPNPs) with increased active surface/volume ratio [72–75]. The synthesis of NPNPs is a physical method in which ultrasonication of the Si substrate is involved. In the first step PSi layers are detached from bulk Si by means of ultrasonicating the Si in a low power ($\approx$ 1 W) in which surface tension mediated disruption takes place. In the second step, sonication is done in a high power ($\approx$ 20 W) to facilitate the particles formation. Obtained NPNPs are stable in water and can be characterized by various methods, as shown in Fig. 16. TEM images show a population of spherical shaped nanoparticles (Fig. 16(a,b)) with an average size of 75 nm, confirmed by DLS measurement
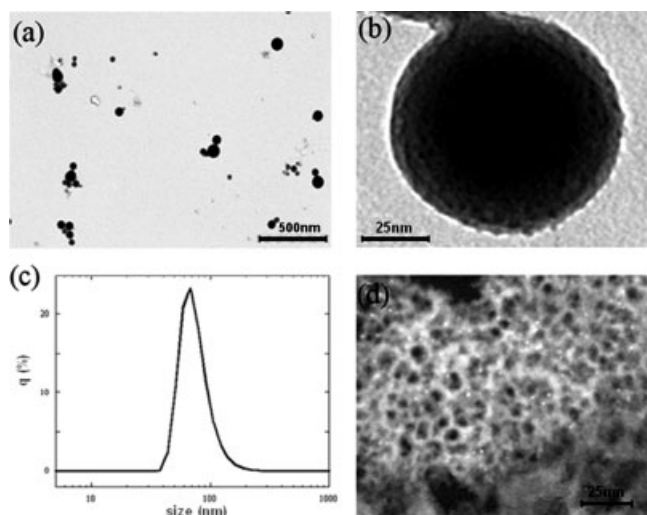
Figure 16 TEM images of round shaped porous Si nanoparticles at low (a) and high (b) magnification. Dynamic Light Scattering (DLS) size distribution (c) of 75 nm NPNPs disperse in water. STEM image (d) which show the nanometer pore structure.

Figure 17 (online color at: www.ann-phys.org) Raman spectra of bulk Si wafer and as prepared NanoPorous Si.

(Fig. 16(c)). The porous structure is evidenced by STEM, with the presence of 2–5 nm pores and Si lattice.

Raman measurements were done on bulk Si wafer and the freshly prepared NPNPs. The spectra were obtained by irradiating the sample with 633 nm laser line for 10 sec with laser power 274 μW. It is clearly observed, from Fig. 17, the Raman spectrum of NPNPs shows (red line) both the sharp peak at 520 cm^{-1} and an asymmetric band on the lower frequency side of it and the intense peak at 520 cm^{-1} is of crystalline Si (black line). The asymmetric band at the lower energy tail confirms the presence of nanocrystalline structures of Si grain [76].

In conclusion, porous Si is a versatile and very attractive material for plasmonic application: it shows an intrinsic SERS activity [77, 78], an excellent biocompatibility, high surface area / volume ratio available for functionalization of the molecules and the possibility to be used as substrate for electroless metal deposition.

5 Conclusion

In this paper, various kind of SERS substrates (i.e. periodic nanograin gold aggregates, nanoantenna, goldcoated anodic porous alumina) and SPPERS device were fabricated using different techniques. In order to test these devices, different molecules, from fluorescent dye to proteins, were deposited by means of chemisorptions technique. The advancement of the fabrication technolo-
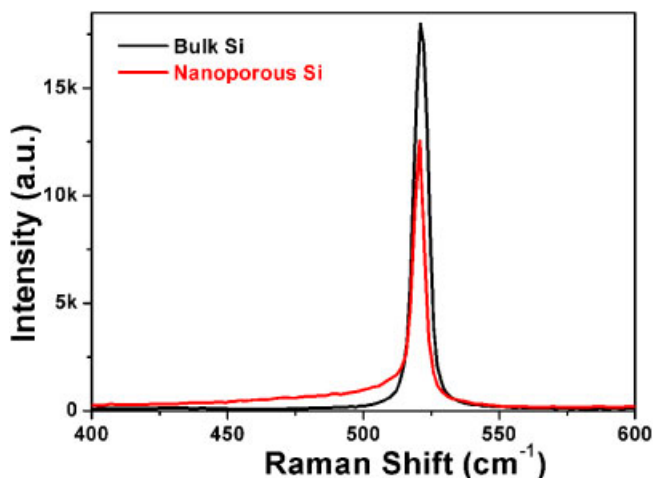
gies enables the reproducibility of SERS device. SERS substrate with periodic nanograin shows the detection sensitivity down to ottomole concentration, whereas the honey-comb structure based SERS substrate found to be an efficient and disposable SERS device with very proficient fluorescence quenching. In addition to these SERS devices, SPPERS device is also reported for which a high electric field is accumulated at the apex of the field due to adiabatic compression. In order to understand the current flow, electric field distribution, etc. for all these devices, theoretical simulations were carried out using the commercial software CST. We have also enlisted the future perspective of plasmonics applications.

References

[1] J. R. Krenn et al., Phys. Rev. Lett. **82**, 2590 (1999).
[2] M. Bosman et al., Nanotechnology **18**, 16505 (2007).
[3] J. Dai, F. ˇCajko, I. Tsukerman, and M. I. Stockman, Phys. Rev. B **77**, 115419 (2008).
[4] J. P. Camden, J. Am. Chem. Soc. **130**(38), 12616 (2008).
[5] S. Nie and S. R. Emory, Science **275** (5303), 1102 (1997).
[6] K. Li, M. I. Stockman, and D. J. Bergman, Phys. Rev. Lett. **91**, 227402 (2003).

[7] M. Moskovits, Rev. Mod. Phys. **57**, 783 (1985).

[8] M. Fleischmann, P. J. Hendra, and A. J. McQuillan, Chem. Phys. Lett. **26**(2), 163 (1974).

[9] D. L. Jeanmaire and R. P. Van Duyne, J. Electroanal. Chem. **84**(1), 1 (1977).

[10] S. Mahajan et al., J. Phys. Chem. C **114**(16), 7242 (2010).

[11] K. Kneipp et al., Phys. Rev. Lett. **78**, 1667 (1997).

[12] S. Shanmukh et al., Nano Lett. **6**(11), 2630 (2006).

[13] J. Hu et al., Analyst **135**, 1084 (2010).

[14] K. Yee, IEEE Trans. Antennas Propag. **14**(3), 302 (1966).

[15] J. Jin, The Finite Element Method in Electromagnetics (Wiley, Chichester, 2002).

[16] R. G. Freeman et al., Science **267**(5204), 1629 (1995).

[17] U. Huebner et al., Microelectron. Eng. **85**(8), 1792 (2008).

[18] M. Tormen et al., Microelectron. Eng. **73–74**, 535 (2004).

[19] S. Cabrini et al., Microelectron. Eng. **78–79**, 11 (2005).

[20] F. Schiappell et al., Microelectron. Eng. **73–74**, 397 (2004).

[21] N. Papasimakis et al., Opt. Express **18**(8), 8353 (2010).

[22] L. Haynes and R. P. Van Duyne, J. Phys. Chem. B **105**, 5599 (2001).

[23] M. J. Banholzer, J. E. Millstone, L. Qin, and C. A. Mirkin, Chem. Soc. Rev. **37**, 885 (2008).

[24] F. De Angelis et al., Nanoscale **3**, 2689 (2011).

[25] F. De Angelis et al., Nature Nanotech. **5**, 67 (2010).

[26] P. E. Sheehan and L. J. Whitman, Nano Lett. **5**(4), 803 (2005).

[27] F. Gentile et al., Microelectron. Eng. **87**, 798 (2010).

[28] F. De Angelis, Nature Photonics **5**, 682 (2011).

[29] M. Chirumamilla et al., Microelectron. Eng. **97**, 189 (2012).

[30] G. Das et al., Biosens. Bioelectron. **24**, 1693 (2009).

[31] G. Das et al., Analyst **137**, 1785 (2012).

[32] R. P. Zaccaria et al., Opt. Exp. **16**, 14812 (2008).

[33] R. P. Zaccaria, S. Shoji, H. B. Sun, and S. Kawata, Appl. Phys. B **93**, 251 (2008).

[34] G. Das et al., Microelectron. Eng. **97**, 383 (2012).

[35] CST, Computer Simulation Technology (CST, Darmstadt, Germany, 2012).

[36] H. J. Lezec and T. Thio, Opt. Express **12**(16), 3629 (2004).

[37] A. D. Rakic, A. B. Djurisic, J. M. Elazar, and M. L. Majewski, Appl. Opt. **37**, 5271 (1998)

[38] G. M. Whitesides, Nature Biotechnol. **21**, 1161 (2003).

[39] L. Razzari et al., Opt. Express **19**, 26088 (2011).

[40] R. Feynman, Caltech Eng. Sci. **23**, 22 (1960).

[41] P. Bharadwaj, B. Deutsch, and L. Novotny, Adv. Opt. Photonics **1**, 438 (2009).

[42] H. A. Atwater and A. Polman, Nature Mater. **9**, 205 (2010).

[43] P. Biagioni, J. Huang, and B. Hecht, Rep. Prog. Phys. **75**, 024402 (2012).

[44] C. F. Bohren and D. R. Huffman, Absorption and Scattering of Light by Small Particles, Chap. 5 (Wiley-VCH, Weinheim, 2004).

[45] E. Vogel, A. Gbureck, and W. Kiefer, J. Mol. Struct. **550**, 177 (2000).

[46] M. Sackmann, S. Bom, T. Balster, and A. Materny, J. Raman Spectrosc. **38**, 277 (2007).

[47] I. Noda, Appl. Spectrosc. **44**(4), 543 (1990).

[48] I. Noda et al., Appl. Spectrosc. **54**(7), 236A (2000).

[49] D. Zhang et al., Anal. Chem. **75**(21), 5703 (2003).

[50] T. Miura Jr. and G. J. Thomas, Proteins: Structure, Function and Engineering, Chap. 24 (Plenum Press, New York, 1995), pp. 55–97.

[51] K. L. Igor, V. E. Vladimir, H. Wei, and M. Xu, Anal. Bioanal. Chem. **381**, 431 (2005).

[52] M. I. Stockman, Phys. Rev. Lett. **93**, 137404 (2004).

[53] A. J. Babadjanyan, N. L. Margaryan, and Kh. V. Nerkararyan, J. Appl. Phys. **87**, 3785 (2000).

[54] X. Chen, V. Sandoghdar, and M. Agio, Opt. Express **18**(10), 10878 (2010).

[55] R. P. Zaccaria et al., Opt. Lett. **37**(4), 545 (2012).

[56] F. De Angelis et al., Opt. Express **19**(22), 22268 (2011).

[57] F. De Angelis et al., Nano Lett. **8**(8), 2321 (2008).

[58] M. Malerba et al., Microlectron. Eng. **97**, 204 (2012).

[59] S. L. Dexheimer, Terahertz Spectroscopy: Principles and Applications, (CRC Press, Boca Raton, 2007).

[60] D. Mittelman, Sensing with THz Radiation (Springer, Berlin, Heidelberg, 2002).

[61] U. Kreibig and M. Vollmer, Optical Properties of Metal Clusters (Springer, New York, 1995).

[62] A. Rice et al., Appl. Phys. Lett. **64**, 1324 (1994).

[63] COMSOL Multiphysics.

[64] L. Vaccari et al., Microelectron. Eng. **83**, 1598 (2006).

[65] M. Gaspari et al., J. Proteome Res. **5**, 1261 (2006).

[66] E. Di Fabrizio, Nanoparticles and Nanostructures for Biophotonic Applications (Intech, Croatia, 2012).

[67] L. Canham, Properties of Porous Silicon (INSPEC, the Institution of Electrical Engineers London, UK, 1997).

[68] H. Foll, M. Christophersen, J. Cartensen, and G. Hassel, Mater, Sci. Eng. R **39**(93), 141 (2002).

[69] Y. Wang et al., J. Phys. Chem. C **112**, 996 (2008).

[70] F. Gentile et al., Biomaterials **31**, 7205 (2010).

[71] P. Granitzer and K. Rumpf, Materials **3**, 943 (2010).

[72] F. De Angelis et al., Nanoscale **2**, 2230 (2010).

[73] A. Pujia et al., Int. J. Nanomedicine **5**, 1005 (2010).

[74] J. H. Park et al., Nature Mater. **8**, 331 (2009).

[75] E. Tasciotti et al., Nature Nanotech. **3**, 152 (2008).

[76] G. Mariotto et al., Appl. Phys. **97**, 113502 (2005).

[77] F. Giorgis et al., Appl. Surf. Sci. **254**, 7494 (2008).

[78] S. Chan et al., Adv. Mater. **15**, 1595 (2003).